



New rare-earth metal germanides with bismuth substitution. Synthesis, structural variations, and magnetism of the $RE[Bi_xGe_{1-x}]_2$ ($RE=Y, Pr, Nd, Sm, Gd-Tm, Lu$) compounds

Jiliang Zhang^a, Benjamin Hmiel^a, Anthony Antonelli^a, Paul H. Tobash^a, Svilen Bobev^{a,*}, Shanta Saha^b, Kevin Kirshenbaum^b, Richard L. Greene^b, Johnpierre Paglione^b

^a Department of Chemistry and Biochemistry, University of Delaware, Newark, DL 19716, USA

^b Department of Physics, University of Maryland, College Park, MD 20742, USA

ARTICLE INFO

Article history:

Received 11 June 2012

Received in revised form

12 July 2012

Accepted 14 July 2012

Available online 23 July 2012

Keywords:

Polar intermetallics

Crystal structure

Single-crystal X-ray diffraction

Rare-earth metals

Magnetism

ABSTRACT

Single-crystals of the novel rare-earth metal-bismuth digermanides with idealized formula $RE[Bi_xGe_{1-x}]_2$ ($RE=Y, Pr, Nd, Sm, Gd-Tm, Lu; x < 0.16(1)$) have been obtained using the Bi-flux technique. Their structures have been established by single-crystal X-ray diffraction; they can be divided into three classes, closely related to the $ZrSi_2$ structure with the space group $Cmcm$ (no. 63). The structural relationship and the variations with the type of the rare-earth metal have been explored and discussed. Temperature-dependent magnetization measurements on the single-crystals reveal magnetic behavior, which have been rationalized based on the mean-field theory. At cryogenic temperatures, the localized $4f$ electrons in most of the compounds exhibit antiferromagnetic ordering, mediated by the conduction electrons via Ruderman–Kittel–Kasuya–Yosida (RKKY) exchange interactions.

© 2012 Elsevier Inc. All rights reserved.

1. Introduction

Rare-earth metal (RE) containing compounds offer a wealth of structures and intriguing properties [1]. They are also excellent candidates for fundamental studies on the factors determining a bonding arrangement of a specific kind, the evolution of the properties within a given structure, and ultimately the structure–property relationships. RE -silicides and RE -germanides are well suited for these types of investigations, and in recent years, such compounds have attracted considerable attention [2]. For instance, in the Dy–Ge binary phase diagram alone [3,4], it has been reported that there are at least eight distinct phases in the narrow compositional range from DyGe to DyGe₂. Such structural diversity suggests that the realization of the multitude of structures is a consequence of multiple cooperating factors, among which topological or electronic considerations are the primary ones [5].

In our previous work, we have demonstrated that one can extend the $ZrSi_2$ structure type (known only for $REGe_2$ when $RE=Tm$ and Lu) to the mid-to-late rare-earth metals by the addition of Sn, forming the series $RE[Sn_xGe_{1-x}]_2$ ($RE=Y, Gd-Tm$) [6]. These orthorhombic structures afforded an unusual

result—Ge and Sn showed a tendency to order on two polyanionic sub-lattices, effectively rendering the compounds in question as nearly stoichiometric (referred to as $RESnGe$ hereafter). The synthesis in these cases was greatly facilitated by the use of the flux techniques [7], which can depress thermal strain (and to some degrees the heterogeneous nucleation) compared with the traditional arc-melting route. However, when we attempted to synthesize analogous compounds with In (notice the small difference in atomic sizes and electronegativity between indium and tin [8]), the RE_2InGe_2 ($RE=Sm, Gd-Ho, Yb$) with the tetragonal U_3Si_2 type structure formed instead [9]. We reasoned that indium is one electron-poorer than Sn, thereby leading to electronic deficiency, which is likely the reason the chemistry did not work. In the next set of experiments, we attempted to determine if the size of the dopant element is a critical factor and considered the existence of $RE[Pb_xGe_{1-x}]_2$ (isoelectronic substitution of Ge with a much heavier element, Pb). These experiments were also unsuccessful and led to the identification of a number of binary germanides, including RE_3Ge_4 ($RE=Y, Gd-Tm$) [4b,10]. At this point, we decided to also explore the electron-richer Bi, which surprisingly produced a very large family of bismuth-substituted digermanides with general formulas $RE[Bi_xGe_{1-x}]_2$ ($RE=Y, Pr, Nd, Sm, Gd-Tm, Lu$). Depending on the nature of the rare-earth metal, they form in three very similar structures, which for the sake of simplicity, are hereafter referred to as $REBiGe$.

* Corresponding author. Fax: +1 302 831 6335.

E-mail address: bobev@udel.edu (S. Bobev).

With the paper, we report the synthesis and the flux-growth of single-crystals of these compounds. Their structures, established from single-crystal X-ray diffraction, and the basic magnetic properties – determined by means of bulk magnetometry – are also discussed.

2. Experimental

2.1. Synthesis

Most of the synthetic work was performed inside an argon-filled glove box or under vacuum. All elements used for synthesis were purchased from Alfa or Aldrich with stated purity greater than 99.9 wt.%. In a typical experiment, a reaction mixture containing the starting materials in the molar ratio RE:Ge:Bi=1:2:8 (RE=La–Sm, Gd–Lu) was loaded into 2 cm³ alumina crucibles. The crucibles were subsequently encapsulated in fused silica tubes, which were flame-sealed under vacuum and heated for reaction in a box furnace. The heating program included a quick ramping to 1273 K at a rate 200 K/h, homogenization for 20 h, and cooling down to 873 K at a rate of 10 K/h. At this temperature the excess molten flux was easily removed by decanting it and the grown crystals were isolated. Details of the metal flux method can be found elsewhere [7].

The Bi-flux technique produced the best results in terms of yield and crystal quality. Due to the very different melting temperatures of the constituent elements and the evaporative loss of bismuth, the REBiGe phase could not be reliably made via arc-melting. Induction melting in sealed tubes worked, but the method was unsuccessful in producing phase-pure material—even after a long time (1–2 weeks) annealing, the induction melted products were multi-phase mixtures and the size/quality of the single-crystals from induction melting was inferior compared to the flux-produced samples.

2.2. X-ray diffraction

Single-crystal X-ray diffraction data were collected on a Bruker SMART CCD-based diffractometer (3-circle goniometer, monochromated MoK α sealed source with $\lambda=0.71073$ Å). The data acquisitions were performed in batch runs at different ω and φ angles with the SMART software [11a]. The raw data were integrated using SAINT [11b] and semiempirical absorption

correction was applied using SADABS [12]. The unit cell parameters were refined using all measured reflections. The structure solution and refinement were done using the SHELXTL package [13]. Refined parameters included the scale factor, the atomic positions with anisotropic displacement parameters (excluding the disordered Ge4 in structures I and II—see below), extinction coefficients (where applicable). Tables 1–3 give further details of the data collection and structure refinement parameters for all structures; final positional and equivalent isotropic displacement parameters for selected ones are listed in Tables 4–6, respectively [14]. Important interatomic distances are provided in Table 7.

X-ray powder diffraction patterns were collected using a Rigaku MiniFlex powder diffractometer (filtered CuK α radiation with $\lambda=1.5418$ Å). The collected powder patterns were primarily used for phase identification of the reaction products, carried out with the aid of the JADE 6.5 software package. The experimental powder X-ray diffraction patterns matched well with those calculated from the single-crystal work.

2.3. Magnetic susceptibility measurements

Field-cooled dc magnetization (M) measurements were conducted using a quantum design magnetic property measurement system (MPMS) SQUID. The measurements were done on single-crystal samples in the direction parallel to the basal plane under an applied field (H) of 500 Oe. The temperature range of the measurements was from 5 K to 300 K. Measurement in the direction normal to the basal plane was also performed on a single-crystal of HoBiGe to examine the effects of crystal anisotropy. Superconductivity has been reported for LuGe₂ [15], thus magnetization measurements (in a SQUID magnetometer down to 1.8 K) and resistivity measurements (in a dilution refrigerator down to 50 mK) of Lu[Bi_xGe_{1-x}]₂ were also carried out.

2.4. Energy-dispersive X-ray spectroscopy (EDX) analysis

EDX analysis was conducted using a JEOL 7400 F electron microscope equipped with an INCA-Oxford energy-dispersive spectrometer. Data were acquired for several areas on the same sample and then averaged. The obtained results (provided as supporting information) are in good agreement with the refined compositions and the elemental-mapping confirms the homogeneity of the samples.

Table 1

Selected single-crystal data collection and structure refinement parameters for RE[Bi_xGe_{1-x}]₂ (RE=Pr, Nd, Sm, Gd, Tb).

	Structure I				
Empirical formula	PrBi _{0.31(1)} Ge _{1.63(1)}	NdBi _{0.28(1)} Ge _{1.62(1)}	SmBi _{0.26(1)} Ge _{1.64(2)}	GdBi _{0.21(1)} Ge _{1.69(2)}	TbBi _{0.14(1)} Ge _{1.74(2)}
Formula weight	323.75	321.21	322.86	324.45	315.01
Space group, Z			Cmcm (no. 63), Z=8		
Radiation, λ			MoK α , 0.71073 Å		
Temperature			–153 °C		
Unit cell parameters					
$a/\text{Å}$	4.147(2)	4.1204(4)	4.0733(7)	4.0404(12)	4.0052(14)
$b/\text{Å}$	31.279(14)	31.070(3)	30.715(5)	30.444(9)	30.213(10)
$c/\text{Å}$	4.303(2)	4.2592(4)	4.2047(7)	4.1629(12)	4.1210(14)
$V/\text{Å}^3$	558.1(4)	545.27(9)	526.03(15)	512.1(3)	498.7(3)
$\rho_{\text{calc}}/\text{g cm}^{-3}$	7.721	7.833	8.153	8.416	8.391
μ/cm^{-1}	538.9	544.6	573.6	595.5	485.9
Data: parameters ratio	477: 30	433: 30	423: 29	421: 29	402: 29
Final R1 ^a ($I > 2\sigma_I$)	R1=0.0317, wR2=0.0642	R1=0.0258, wR2=0.0589	R1=0.0214, wR2=0.0484	R1=0.0276, wR2=0.0525	R1=0.0233, wR2=0.0535
Largest diff. peak and hole/ $e^- \text{Å}^{-3}$	1.40 and –1.50	1.71 and –1.40	1.40 and –1.57	3.04 and –3.01	1.90 and –2.33

^a $R1 = \sum ||F_o| - |F_c|| / \sum |F_o|$; $wR2 = [\sum [w(F_o^2 - F_c^2)]^2 / \sum [w(F_o^2)]^2]^{1/2}$, where $w = 1/[\sigma^2 F_o^2 + (A \cdot P)^2 + (B \cdot P)]$, and $P = (F_o^2 + 2F_c^2)/3$; A and B weight coefficients.

Table 2
Selected single-crystal data collection and structure refinement parameters for RE[Bi_xGe_{1-x}]₂ (RE=Dy, Ho, Y).

	Structure II		
	DyBi _{0.09(1)} Ge _{1.76(1)}	HoBi _{0.08(1)} Ge _{1.77(2)}	YBi _{0.11(1)} Ge _{1.75(2)}
Empirical formula	DyBi _{0.09(1)} Ge _{1.76(1)}	HoBi _{0.08(1)} Ge _{1.77(2)}	YBi _{0.11(1)} Ge _{1.75(2)}
Formula weight	309.93	310.22	238.33
Space group, <i>Z</i>		<i>Cmcm</i> (no. 63), <i>Z</i> =8	
Radiation, λ		MoK α , 0.71073 Å	
Temperature		–153 °C	
Unit cell parameters			
<i>a</i> /Å	4.1120(10)	4.0951(8)	4.128(5)
<i>b</i> /Å	29.917(8)	29.799(6)	30.08(3)
<i>c</i> /Å	3.9234(10)	3.9159(8)	3.934(5)
<i>V</i> /Å ³	482.7(2)	477.85(16)	488.6(10)
ρ_{calc} /g cm ⁻³	8.530	8.624	6.479
μ /cm ⁻¹	588.94	603.97	522.06
Data: parameters ratio	391: 29	392: 29	385: 29
Final <i>R</i> ^a (<i>I</i> > 2 σ _{<i>i</i>})	<i>R</i> 1=0.0242, <i>wR</i> 2=0.0536	<i>R</i> 1=0.0191, <i>wR</i> 2=0.0450	<i>R</i> 1=0.0347, <i>wR</i> 2=0.0801
Largest diff. peak and hole/e ⁻ Å ⁻³	1.65 and –1.65	2.08 and –1.57	1.88 and –2.29

^a $R1 = \sum ||F_o| - |F_c|| / \sum |F_o|$; $wR2 = [\sum [w(F_o^2 - F_c^2)^2] / \sum [w(F_o^2)^2]]^{1/2}$, where $w = 1 / [\sigma^2 F_o^2 + (A \cdot P)^2 + (B \cdot P)]$, and $P = (F_o^2 + 2F_c^2) / 3$; *A* and *B* weight coefficients.

Table 3
Selected single-crystal data collection and structure refinement parameters for RE[Bi_xGe_{1-x}]₂ (RE=Er, Tm, Lu).

	Structure III		
	ErBi _{0.16(1)} Ge _{1.84(1)}	TmBi _{0.11(1)} Ge _{1.89(1)}	LuBi _{0.06(1)} Ge _{1.94(1)}
Empirical formula	ErBi _{0.16(1)} Ge _{1.84(1)}	TmBi _{0.11(1)} Ge _{1.89(1)}	LuBi _{0.06(1)} Ge _{1.94(1)}
Formula weight	334.26	329.11	327.65
Space group, <i>Z</i>		<i>Cmcm</i> (no. 63), <i>Z</i> =4	
Radiation, λ		MoK α , 0.71073 Å	
Temperature		–153 °C	
Unit cell parameters			
<i>a</i> /Å	4.0475(11)	4.0230(4)	3.9935(4)
<i>b</i> /Å	15.969(5)	15.814(2)	15.616(2)
<i>c</i> /Å	3.8983(11)	3.8785(4)	3.8570(4)
<i>V</i> /Å ³	251.97(12)	246.74(4)	240.53(4)
ρ_{calc} /g cm ⁻³	8.811	8.860	9.048
μ /cm ⁻¹	655.42	659.25	684.53
Data: parameters ratio	201: 15	199: 15	196: 15
Final <i>R</i> ^a (<i>I</i> > 2 σ _{<i>i</i>})	<i>R</i> 1=0.0176, <i>wR</i> 2=0.0383	<i>R</i> 1=0.0198, <i>wR</i> 2=0.0483	<i>R</i> 1=0.0163, <i>wR</i> 2=0.0359
Largest diff. peak and hole/e ⁻ Å ⁻³	1.84 and –1.31	1.66 and –2.07	1.40 and –1.18

^a $R1 = \sum ||F_o| - |F_c|| / \sum |F_o|$; $wR2 = [\sum [w(F_o^2 - F_c^2)^2] / \sum [w(F_o^2)^2]]^{1/2}$, where $w = 1 / [\sigma^2 F_o^2 + (A \cdot P)^2 + (B \cdot P)]$, and $P = (F_o^2 + 2F_c^2) / 3$; *A* and *B* weight coefficients.

Table 4
Atomic coordinates and equivalent isotropic displacement parameters U_{eq} ^a (Å²) of RE[Bi_xGe_{1-x}]₂ (RE=Pr and Gd)—two subtly different representatives of structure I.

Atom	Site	Occup.	<i>x</i>	<i>y</i>	<i>z</i>	U_{eq}
PrBiGe						
Pr1	4c	1	0	0.4418(1)	1/4	0.009(1)
Pr2	4c	1	0	0.8319(1)	1/4	0.009(1)
Ge1/Bi	4c	0.38/0.62(1)	0	0.2495(1)	1/4	0.018(1)
Ge2	4c	1	0	0.0908(1)	1/4	0.013(1)
Ge3	4c	1	0	0.6396(1)	1/4	0.010(1)
Ge4a	8f	0.21(1)	0	0.0118(2)	0.127(2)	0.013(1)
Ge4b	4c	0.35(1)	0	0.0157(2)	1/4	0.013(1)
Ge4c	4a	0.10(1)	0	0	0	0.013(1)
GdBiGe						
Gd1	4c	1	0	0.4411(1)	1/4	0.009(1)
Gd2	4c	1	0	0.8308(1)	1/4	0.009(1)
Ge/Bi1	4c	0.57/0.43(1)	0	0.2494(1)	1/4	0.017(1)
Ge2	4c	1	0	0.0903(1)	1/4	0.012(1)
Ge3	4c	1	0	0.6419(1)	1/4	0.010(1)
Ge4a	8f	0.23(1)	0	0.0082(2)	0.088(1)	0.016(1)
Ge4b	4c	0.33(1)	0	0.0134(2)	1/4	0.016(1)

^a U_{eq} is defined as one third of the trace of the orthogonalized U_{ij} tensor.

Table 5
Atomic coordinates and equivalent isotropic displacement parameters U_{eq} ^a (Å²) of Dy[Bi_xGe_{1-x}]₂—a representative of structure II.

Atom	Site	Occup.	<i>x</i>	<i>y</i>	<i>z</i>	U_{eq}
Dy1	4c	1	0	0.4403(1)	1/4	0.010(1)
Dy2	4c	1	0	0.6709(1)	1/4	0.010(1)
Ge1/Bi	4c	0.80/0.20(1)	0	0.2489(1)	1/4	0.015(1)
Ge2	4c	1	0	0.0911(1)	1/4	0.013(1)
Ge3	4c	1	0	0.8552(1)	1/4	0.011(1)
Ge4a	8f	0.20(1)	0	0.0071(2)	0.097(1)	0.010(1)
Ge4b	4c	0.30(1)	0	0.0119(2)	1/4	0.010(1)

^a U_{eq} is defined as one third of the trace of the orthogonalized U_{ij} tensor.

3. Results

3.1. Synthesis and structures

The discussed REBiGe compounds can be readily synthesized from reactions of the corresponding rare-earth metals and

Table 6

Atomic coordinates and equivalent isotropic displacement parameters U_{eq} (\AA^2) of $\text{Tm}[\text{Bi}_x\text{Ge}_{1-x}]_2$ —a representative of structure **III**.

Atom	Site	Occup.	x	y	z	U_{eq}
Tm	4c	1	0	0.8974(1)	1/4	0.008(1)
Ge1/Bi	4c	0.89/0.11(1)	0	0.2527(1)	1/4	0.013(1)
Ge2	4c	1	0	0.5525(1)	1/4	0.009(1)

^a U_{eq} is defined as one third of the trace of the orthogonalized U_{ij} tensor.

Table 7

Selected interatomic distances (\AA) in $\text{RE}[\text{Bi}_x\text{Ge}_{1-x}]_2$ ($\text{RE}=\text{Pr}$, Gd, Dy, and Tm). M represents the mixed occupied Ge and Bi position.

Atomic pair	Distance, \AA	Atomic pair	Distance, \AA
PrBiGe		GdBiGe	
Pr1–Ge2 ($\times 4$)	3.157(1)	Gd1–Ge2 ($\times 4$)	3.047(1)
Pr1–Pr2 ($\times 2$)	4.015(2)	Gd1–Ge3 ($\times 2$)	3.271(2)
Pr1–Pr1 ($\times 2$)	4.147(2)	Gd1–Gd2 ($\times 2$)	3.919(1)
Pr2–Ge3 ($\times 4$)	3.118(1)	Gd1–Gd1 ($\times 2$)	4.040(1)
Pr2–Ge2 ($\times 2$)	3.238(2)	Gd2–Ge3 ($\times 4$)	3.012(1)
Pr2–M ($\times 2$)	3.308(1)	Gd2–Ge2 ($\times 2$)	3.180(2)
Pr2–Pr2 ($\times 2$)	4.147(2)	Gd2–M ($\times 2$)	3.188(2)
M–M ($\times 4$)	2.9881(9)	Gd2–Gd2 ($\times 2$)	4.040(1)
Ge2–Ge3 ($\times 2$)	2.576(2)	M–M ($\times 4$)	2.893(1)
Ge3–Pr1 ($\times 2$)	3.333(2)	Ge2–Ge3 ($\times 2$)	2.555(2)
DyBiGe		TmBiGe	
Dy1–Ge2 ($\times 4$)	2.9934(7)	Tm–Ge ($\times 4$)	2.9042(4)
Dy1–Ge3 ($\times 2$)	3.273(1)	Tm–M ($\times 2$)	3.0464(7)
Dy1–Dy2 ($\times 2$)	3.864(1)	Tm–M ($\times 2$)	3.0646(9)
Dy1–Dy1 ($\times 2$)	3.923(1)	Tm–Ge ($\times 2$)	3.1728(9)
Dy2–Ge3 ($\times 4$)	2.9474(6)	Tm–Tm ($\times 2$)	3.7811(5)
Dy2–M ($\times 2$)	3.099(1)	M–M ($\times 4$)	2.795(1)
Dy2–Ge2 ($\times 2$)	3.151(1)	Ge–Ge ($\times 2$)	2.554(2)
Dy2–Dy2 ($\times 2$)	3.923(1)		
M–M ($\times 4$)	2.8425(5)		
Ge2–Ge3 ($\times 2$)	2.535(1)		

germanium in molten Bi. These syntheses afforded the title compounds in high yields and as nearly single-phase products for all rare-earth metals except La, Ce, Eu and Yb. Since the crystals were grown in a bismuth-rich solution, we can speculate that the Bi-content in $\text{RE}[\text{Bi}_x\text{Ge}_{1-x}]_2$ is not likely to be increased beyond the observed. This thinking is supported by variations of the amount of Bi used as a flux which produced no statistically significant changes. Furthermore, it can also be suggested that the $\text{RE}[\text{Bi}_x\text{Ge}_{1-x}]_2$ phases are meta-stable since the attempts to prepare them by means of stoichiometric reactions to study their phase-width always showed that the binary RE_5Ge_3 or REGe_{2-x} phases as major products. This is not surprising because they are high-melting and thermodynamically stable phases according to the binary diagrams [3].

Although the reported bismuth–germanides are structurally similar to the previously identified families of tin–germanides [16], we must note that the Bi amount is much smaller than Sn, most likely due to the atom mismatch. Additionally, there is a dependence of the Bi contents on the size of the RE elements, as shown in Fig. 1. One can see that the Bi content follows the lanthanide contraction; the latter is also the likely reason for the existence of the three slightly different structures—structure **I** realized for RE=Pr, Nd, Sm, Gd, and Tb; structure **II** adopted by RE=Y, Dy, Ho; and structure **III** realized for RE=Er, Tm, and Lu.

All powder X-ray diffraction patterns of the raw materials were indexed in the orthorhombic structure with space group $Cmcm$ (no. 63). EDX analyses revealed that only very small amounts of Bi are present in the materials—in contrast with the RESnGe tin–germanides (ZrSi_2 type [17]), which were found to be

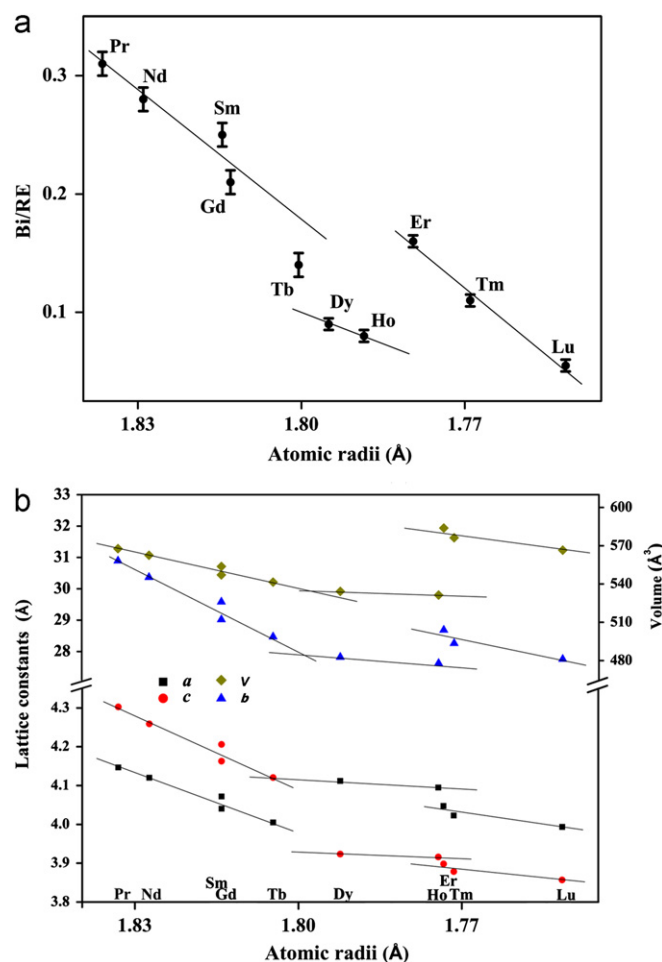


Fig. 1. (a) Bi content (expressed as the ratio of Bi/RE) as a function of the atomic radii of the rare-earth metal atoms. (b) Variation of unit-cell size as a function of the atomic radii of the rare-earth metal atom. For convenience, RE=Er, Tm and Lu, the unit cell was doubled along the b -axis.

nearly equiatomic [6]. However, we had also previously identified $\text{RE}[\text{Sn}_x\text{Ge}_{1-x}]_2$ ($\text{RE}=\text{Gd}$, Tb) [16], where the structure was slightly different (doubled unit cell based on ZrSi_2 like slabs) and Sn-leaner, suggesting a possible isomorphism with the latter. This observation prompted us to establish the structures from single-crystal X-ray diffraction data—the refinements were in good agreement with the structural model (and the chemical make-up derived from EDX) only for RE=Y, Dy, Ho. The single-crystal X-ray diffraction also showed that the structure of the REBiGe compounds when RE=Pr, Nd, Sm, Gd, and Tb is subtly different, albeit also a superstructure of the ZrSi_2 type [17], while the structures of $\text{RE}[\text{Bi}_x\text{Ge}_{1-x}]_2$ for the very late (and spatially smallest) rare-earth metals Er, Tm, and Lu are essentially those of the corresponding REGe_2 phases with a small admixture of Ge and Bi.

The parameters of the single-crystal data collection and refinements of each structure are summarized in Tables 1–3; schematic representations of the three structures are projected in Figs. 2–4, respectively. In addition to the Bi–Ge substitution on one of the sites, we must point out that there is some positional Ge-atom disorder in structures **I** and **II** (discussed next); the poorly localized electron density in the PrBiGe, NdBiGe and SmBiGe structures is best modeled by three disordered sites (Table 4), whilst we refined in the formally isotopic GdBiGe and TbBiGe structures with only two disordered sites. Some relevant interatomic distances are given in Table 7.

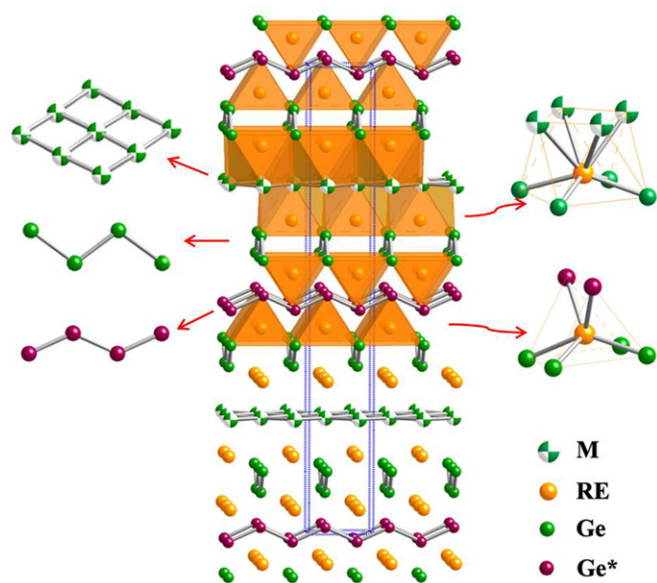


Fig. 2. Schematic representation of structure **I**, viewed approximately along the *a*-axis: *M* represents the mixed occupied Ge and Bi position, and *Ge** stands for the disordered Ge chain. The basic units (rare-earth metal polyhedra, ${}^2_{\infty}[M]$ square sheets, and ${}^1_{\infty}[\text{Ge}]$ zig-zag chains) are highlighted. On-line colors: rare-earth metal atoms are represented as gold spheres, the germanium atoms in the ordered ${}^1_{\infty}[\text{Ge}]$ zig-zag chains are drawn as green spheres, while the disordered Ge chain is shown in dark red. The ${}^2_{\infty}[M]$ square sheets, made up of mixed occupied Ge and Bi atoms are shown with white-green spheres. The unit cell is outlined. (For interpretation of the references to color in this figure caption, the reader is referred to the web version of this article.)

As shown in Figs. 2–4, all structures are made up of “square”-sheets of mixed Ge/Bi atoms (denoted as ${}^2_{\infty}[M]$ in the plots) and ${}^1_{\infty}[\text{Ge}_2]$ zig-zag chains. The polyanionic fragments are separated by *RE* atoms, commonly coordinated by eight neighbors (four Ge atoms and four Bi/Ge atoms). The shape of this coordination polyhedron is a distorted square antiprism (ideal point symmetry D_{4d}). The antiprisms are connected by sharing triangular faces formed by one *M* atom and two Ge atoms in layers normal to the longest axis in each structure, the *b*-axis. Such layers are further paired by common edges in the ${}^2_{\infty}[M]$ square sheets, making up double-slabs common to all structures (see Fig. 5). Another kind of *RE* atom in structure **I** is capped by six atoms (four Ge atoms plus two disordered Ge atoms) seated in the corners of a triangular prism, quite distorted from the ideal symmetry of D_{3h} . These triangular prisms are also associated by shared edges in the layers normal to the long *b*-axis. In structure **II**, the disordered Ge chains are running in a direction orthogonal to the one in structure **I**. Therefore, the second crystallographically unique *RE*-atom in this arrangement can be thought to be at the center of an irregular hexagonal prism (Fig. 3).

The presence of the disordered Ge chains is what differentiates structures **I** and **II** from structure **III**. The latter is devoid of positional Ge disorder, only Bi/Ge substitution is observed at the site describing the square-sheets. This can be explained by the tendency of Bi to favor hypervalent bonding as a result of the inert $6s^2$ pair of electrons [18]. Similar “coloring” (i.e., preferred occupation by a given element) of the polyanionic sub-structure was also noted for the isostructural RESnGe compounds [6,16]. For structures **I** and **II**, the very same preference of Bi to occupy the square sheets is evident. The difference between the latter two and structure **III** is the additional disordered zig-zag chain, which requires doubling the periodicity along their *b*-axes (Tables 1–3) [19]. As stated already, the orientation of these disordered zig-zag chains is the major difference between structures **I** and **II**.

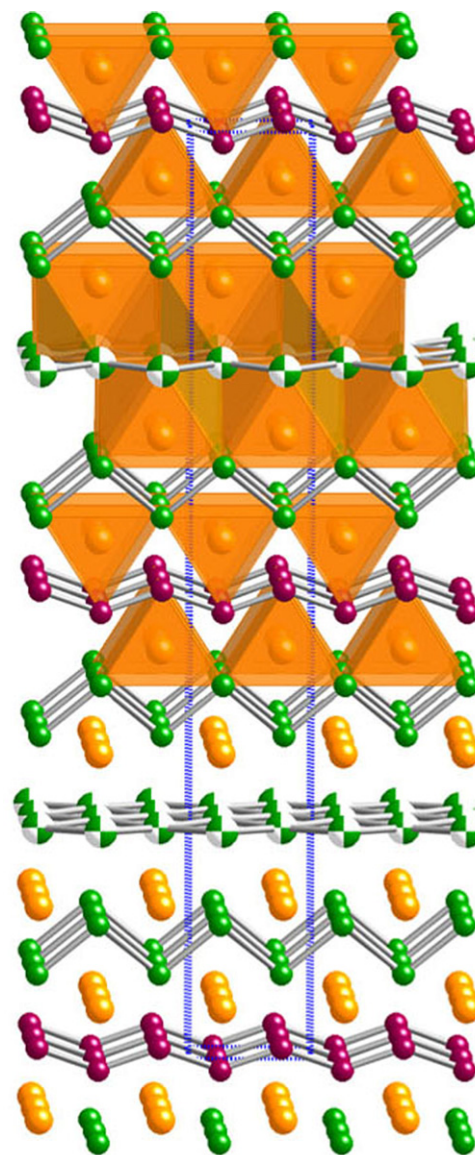


Fig. 3. Schematic representation of structure **II**, viewed approximately along the *a*-axis. On-line colors: rare-earth metal atoms are represented as gold spheres, the germanium atoms in the ordered ${}^1_{\infty}[\text{Ge}]$ zig-zag chains are drawn as green spheres, while the disordered Ge chain is shown in dark red. The ${}^2_{\infty}[M]$ square sheets, made up of mixed occupied Ge and Bi atoms are shown with white-green spheres. The unit cell is outlined. (For interpretation of the references to color in this figure caption, the reader is referred to the web version of this article.)

The electron density defining these disordered zig-zag chains in structures **I** and **II** is smeared and difficult to ascribe to a single site. We modeled the disorder in several different ways, and the best refinements are presented in Tables 4–5. Notice that most of the obtained interatomic distances within the chains are not physical, had there been no disorder at the Ge4 sites in structures **I** and **II**, neighboring Ge4 atoms would be separated by about 2.3 Å or less, suggesting vacancies at that position as well. Notice that the unconstrained refinements we have provided do confirm that $\text{RE}[\text{Bi}_x\text{Ge}_{1-x}]_2$ ($\text{RE}=\text{Y}, \text{Pr}, \text{Nd}, \text{Sm}, \text{Gd-Ho}$) are slightly sub-stoichiometric.

3.2. Magnetism

The temperature dependence of the magnetization of samples of REBiGe is plotted in Figs. 6–8. The measurements were taken

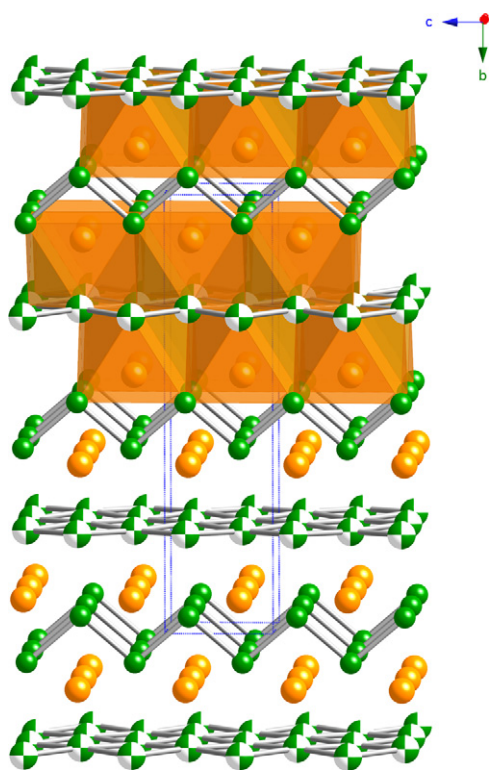


Fig. 4. Schematic representation of structure **III**, viewed approximately along the *a*-axis. On-line colors: rare-earth metal atoms are represented as gold spheres, the germanium atoms in the $^1_{\infty}[\text{Ge}]$ zig-zag chains are drawn as green spheres, while the $^2_{\infty}[\text{M}]$ square sheets, made up of mixed occupied Ge and Bi atoms are shown with white-green spheres. The unit cell is outlined. (For interpretation of the references to color in this figure caption, the reader is referred to the web version of this article.)

on single-crystalline material and as seen from Fig. 8, there is an apparent anisotropy in the magnetization response, but not in ordering temperature. As shown in the figures, all measured samples exhibit low-temperature antiferromagnetic behaviors excluding NdBiGe and TmBiGe. A closer view at the low-temperature region (inset on left hand in the figure of Pr compound) revealed the two-stage transition existed in PrBiGe compound. All experimentally determined Néel temperatures are listed in Table 8. The virtually perfect linearity, seen from inset plots of the inverse molar magnetic susceptibility against temperature, indicates that all samples follow the Curie–Weiss law [20] in the paramagnetic region, except SmBiGe. By fitting these data using Curie–Weiss law, effective moment p_{eff} and paramagnetic Curie temperature θ were obtained and also summarized in Table 8. Compared with the other compounds, SmBiGe shows a much smaller magnetic susceptibility value, determined as $\sim 10^{-5}$ – 10^{-6} emu/g at high temperature. It is close in value to the diamagnetic susceptibility and Van Vleck (polarization) paramagnetic susceptibility terms [20]. Thus, these two contributions, neglected in Curie–Weiss law [20], must be taken into consideration in the case of SmBiGe. According to the mean field approximation, the paramagnetic susceptibility $\chi(T)$ of a metallic samarium compound should be of the following form below room temperature [21]:

$$\chi(T) = \chi_0 + D/(T - \theta) \quad (1)$$

where χ_0 is the temperature-independent susceptibility and D is the effective Curie constant. The susceptibility of SmBiGe shown in Fig. 6 can be well fitted using Eq. (1) with the parameters $\chi_0 = 1.89 \times 10^{-6}$ emu/g, $\theta = -21.4$ K and $D = 235 \times 10^{-6}$ emu/g. The determined effective moment p_{eff} from the D is $0.76 \mu_{\text{B}}$.

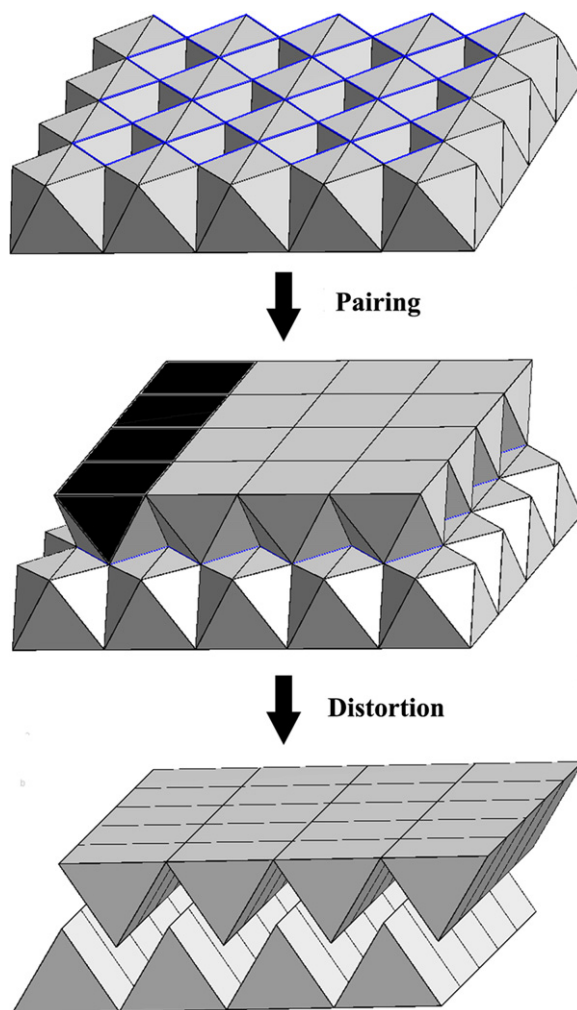


Fig. 5. A scheme showing the coupling and distortion of the square-antiprismatic layer: bright (blue) lines mark shared edges on coupling and the dark volume outlines distorted triangle prisms existed in the former three structures. (For interpretation of the references to color in this figure caption, the reader is referred to the web version of this article.)

4. Discussion

4.1. Structural correlations

Paired layers of square antiprisms are common elements in many structures of compounds with $\text{RE}T_2$ formulas ($T = \text{p-block elements or their mixtures}$) [22]. Thus, it is not surprising that structure **III** (precisely $\text{RE}T_2$) is built by the stacking of $^2_{\infty}[\text{REMGe}]$ layers with antiprismatic geometry. In contrast, the other REBiGe compounds have compositions $\text{RE}T_{\sim 1.9}$. As discussed previously, the deviation from the ideal stoichiometry (as in most other cases) reduces the symmetry in (at least) one direction, which requires the doubled size of unit cell in that direction. This is exactly the case of structures **I** and **II**, as shown in Tables 1 and 2. The variation of structural parameters with the size of the rare-earth atoms is plotted in Fig. 1. The variation of lattice constants a and c reveals a change point through DyBiGe, in coincidence with the rotation between the $^2_{\infty}[\text{REMGe}]$ double layer and $^2_{\infty}[\text{REGe}_2]$ double layers. Such rotation also induces the rearrangement of two kinds of $^1_{\infty}[\text{Ge}_2]$ chains from perpendicular to parallel. Since structure appears to be dependent not only on the geometric factors (lanthanide contraction), but also the Bi contents (electronic structure), one might argue that the synergy between the two effects is of importance.

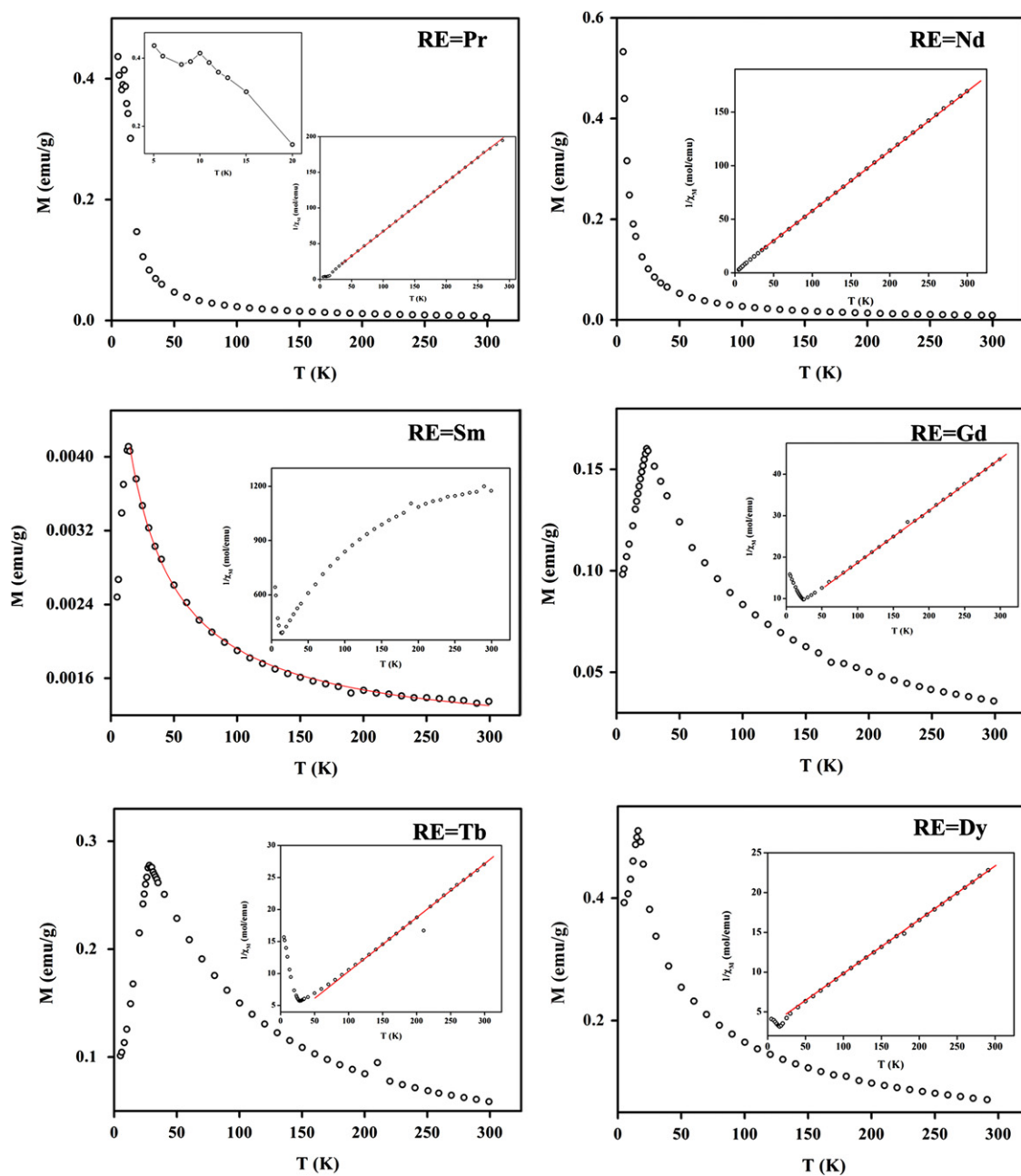


Fig. 6. Field cooled magnetization data gather under an applied field of 500 Oe for the REBiGe compounds with structures I and II. The insets show the temperature dependence of inverse molar magnetic susceptibility $1/\chi_M$. All compounds except SmBiGe exhibit Curie-Weiss paramagnetic behaviors.

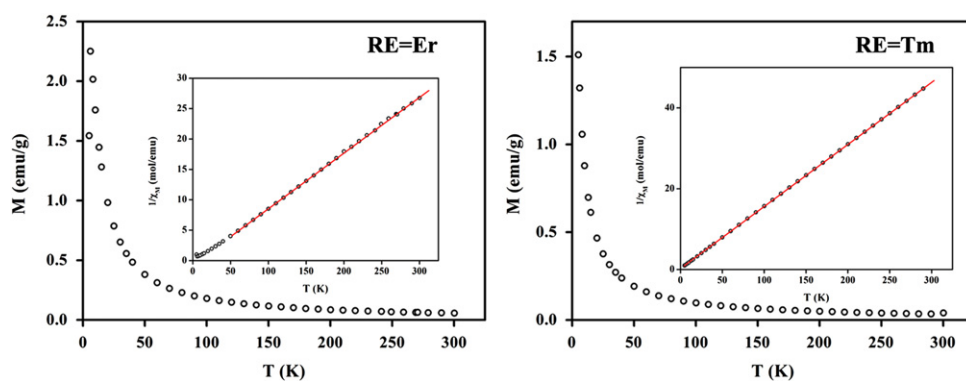


Fig. 7. Field cooled magnetization data gather under an applied field of 500 Oe for the REBiGe compounds with structure III. The inverse molar magnetic susceptibility is shown in the insets.

4.2. Magnetism

A linear relationship between measured Néel temperature and de Gennes factors ($G=J(J+1)(g-1)^2$, where J is the total angular momentum and g is the Landé factor [20]) is visible in Fig. 9, which suggests the Ruderman–Kittel–Kasuya–Yosida (RKKY) exchange interaction [23]. There are four compounds with transition temperatures lower than that can be expected from the linear fit in the nine measured samples. Lower Néel temperatures of Tb- and Er-containing compounds have also been observed in TbZn₁₂ and ErZn₁₂ compounds, which has been attributed to only one crystal field doublet being involved in the magnetic transition [24].

We also note the presence of multiple successive transitions in PrBiGe, as shown in Fig. 6. For antiferromagnets, there are at least two sets of magnetic sub-lattices against each other [25]. It is not necessary for these two sub-lattices to order simultaneously (in low fields or spontaneously), especially in compounds with large crystal anisotropy. This generally leads to two separated magnetic transitions, as observed in some digermanides [4b,26]. However, the separated transitions are often hidden by the applied field and hard to detect. In SmSnGe, for instance, only one transition was revealed by the magnetization, but the second transition was clearly seen in the measurement of the specific heat [6]. In this view, the REBiGe compounds can show two separate transitions or only one transition dominated by either sub-lattice depending on their magnetic structure. The latter can be illustrated schematically using two

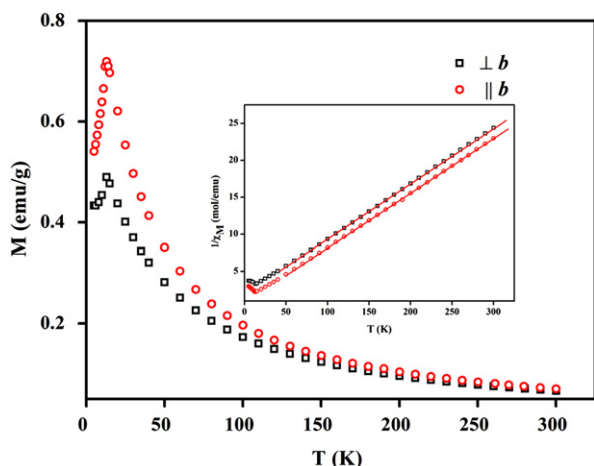


Fig. 8. Field cooled magnetization data of oriented single-crystals of HoBiGe, gathered under an applied field of 500 Oe. Two data sets with applied field in a direction parallel and normal to the ac -plane are compared. The inset shows the temperature dependence of the inverse molar magnetic susceptibility $1/\chi_M$.

sub-lattices model [25]. The antiferromagnetic arrangement in rare-earth metal compounds is generally non-colinear, as depicted by the inset in Fig. 9. The sub-lattice on the right-hand side is preferentially aligned with the direction of the magnetic field, and determines the ordering temperature—it can be either of two, dependent on the compound. Based on this, one can reason that the Néel temperatures out of the line may follow another rule with the de Gennes factor (see the dotted line in Fig. 9). The estimated ordering temperature of NdBiGe and TmBiGe from the fitting is very reasonable around 5 K and 4 K, respectively. As mentioned earlier, the partial substitution of Ge in the sheets does not affect the RE sub-lattices significantly. Thus, the similar magnetic interaction is expected in the RESnGe compounds, and the transition temperatures of these compounds were also plotted in the Fig. 9 for comparison [16]. Three of them show identical transition temperature with the corresponding REBiGe compounds.

Following the notion that RKKY exchange interaction exists in all compounds, it is instructive to estimate the coupling constant to better understand their magnetic interactions. For typical RE-intermetallics, obeying the paramagnetic Curie–Weiss law, the effective moment can be calculated using the expression [21]

$$p_{eff} = gJ(J+1)^{1/2}[1+2J(0)\rho(g-1)/g] \quad (2)$$

where $J(0)$ is the zero wave-vector component of the s–f coupling constant $J(\mathbf{q})$ [26b] and ρ is the density of conduction electron states per atom for one spin direction. From the experimental value of p_{eff} , $J(0)\rho$ was deduced and listed in Table 8. For SmBiGe,

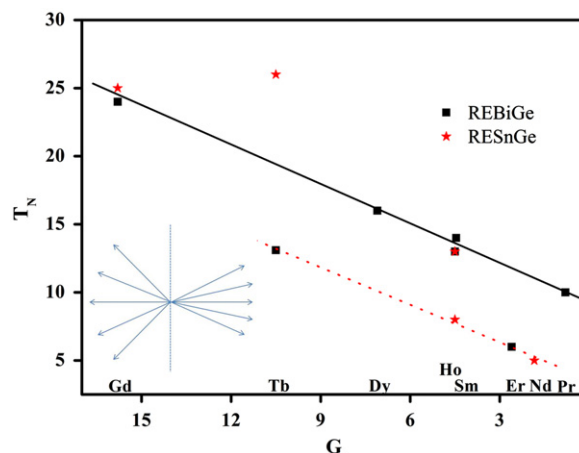


Fig. 9. Néel temperatures of the REBiGe and RESnGe compounds, plotted as a function of the corresponding rare-earth metal de Gennes factors. The inset shows the projection of magnetic ordering on the basal plane schematically.

Table 8
Magnetic parameters for $RE[Bi_xGe_{1-x}]_2$.

Compounds	Ordering	$g\sqrt{J(J+1)}$	p_{eff} (μ_B)	θ (K)	T_N (K)	$J(0)\rho$	J_{ff}/k (K) ^a
PrBiGe	AFM	3.58	3.43	−0.3	10	0.0816	−0.62
NdBiGe	AFM	3.62	3.78	−2.8	≤ 5	−0.0571	−2.24
SmBiGe	AFM	0.85	0.76	−21.4	14	0.0350	−7.39
GdBiGe	AFM	7.94	7.88	−38.8	23	−0.0075	−3.69
TbBiGe	AFM	9.72	9.79	−24.9	13	0.0105	−3.55
DyBiGe	AFM	10.63	10.86	−43.6	16	0.0434	−9.25
HoBiGe	AFM ($\perp b$)	10.6	10.34	−24.7	13	−0.0625	−8.22
HoBiGe	AFM ($\parallel b$)	10.6	10.42	−10.9	13	−0.0417	−3.65
ErBiGe	AFM	9.58	9.34	7.08	6	−0.0763	4.16
TmBiGe	AFM	7.56	7.23	−2.1	≤ 5	−0.1536	−2.72

^a J_{ff}/k (K) is the exchange constant.

^b Single-crystal in two orientations with respect to basal plane.

the $J(0)\rho$ can be obtained using the parameters from Eq. (1) based on the methods in Ref. [21]. These obtained coupling constants show reasonable values with oscillating signs. The positive sign indicates a consistent increment in the size of the paramagnetic moment while the negative claims a reduction, as confirmed by the heavy *RE*-compounds (Table 8). The variation of paramagnetic moment in light *RE*-compounds not in agreement with the coupling constant, which was also met in other structures, may result from the large ionic anisotropy or complexly structural behaviors [24b].

The RKKY mediated Heisenberg exchange interaction between *RE* spins is expressed as the form [21]

$$H_S = -\sum_{i,j} A_{ij} S_i \cdot S_j \quad (3)$$

where S is the spin of the local moment, and A_{ij} are the coefficients of the interactions. The exchange constant for the interaction is the integration $J_{ff} = \sum_{i \neq j} A_{ij}$, and can be estimated following Ref. [21]. The negative values of the obtained exchange constant in Table 8 indicated the antiferromagnetic arrangement of *RE* ions clearly. The positive exchange constant of ErBiGe is likely ascribed to crystal field effects dominating over exchange as suggested by Stewart [24a].

According to the two sub-lattices model [25], spins in one sub-lattice interact with spins in another sub-lattice by an antiferromagnetic coupling $-J$ ($J > 0$). Besides the antiferromagnetic interaction, the spins also interact with spins within the same sub-lattice by a ferromagnetic coupling, $+J'$. If $J' \sim 0$ or $\ll J$, it yields $T_N = \theta$ for the simple antiferromagnet. If T_N was not equal to θ , the two exchange couplings can be estimated using the relationship [27]

$$\frac{J'}{J} = \frac{T_N + \theta}{T_N - \theta} \quad (4)$$

Ferromagnetic coupling is observed in the basal plane of all measured compounds. There is a special one, PrBiGe, which shows ferromagnetic coupling comparable with antiferromagnetic coupling. A transition from antiferromagnetism to ferromagnetism is ready if the ferromagnetic coupling was enhanced by change of structures or elements. The conclusion is confirmed by ferromagnetic ordering in PrGe_{2-x} [26b] and Pr(CuGe)_{1.9} [28]. The HoBiGe compound shows a negligible J' in the direction normal to the basal plane, which suggests the purely antiferromagnetic coupling in the *b*-axis direction.

Although the *RE*-lattice is not subjected to significant change upon the structural transformation from square antiprisms to triangle prisms, it is distinguished in Fig. 9 that all measured compounds of structure III show low transition temperature lying on the dotted line while other compounds show relatively high temperature with the solid line. It is not the *s*-*f* coupling causing the change because of their close strength listed in Table 8. Therefore, it is likely the formation of triangular prisms affects the transition temperature to some extent. Despite the similar *s*-*f* coupling strength and no magnetic contribution, non-magnetic elements can also produce different effects on magnetic behaviors by crystal field effects [29]. According to the theory, the *4f* band of *RE* in the field of D_{4h} splits into seven items: $A_{1g} + A_{1g} + B_{1g} + A_{2g} + E_g + B_{2g} + E_g$, while the *4f* band in the field of D_3 splits into six items: $A_1 + E + A_2 + E + A_1 + E$ [30]. Although the amplitude of splitting is dependent on the crystal-field strength, the symmetric change does indicate a broadening *4f* band in square antiprisms compared with triangular prisms. As a result, the compounds with triangular prisms generally show an elevated transition temperature compared with compounds consisting of only square antiprisms, as depicted by the two lines in Fig. 9.

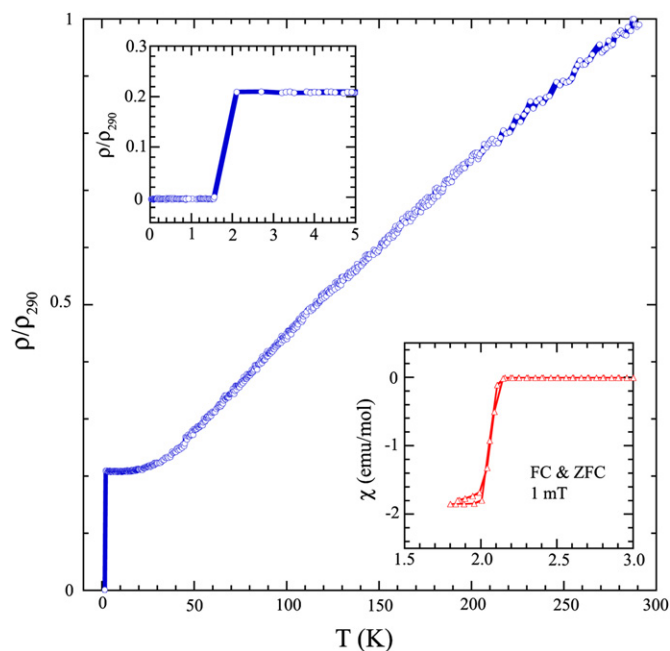


Fig. 10. Temperature dependence of the electrical resistivity LuBi_{0.06(1)}Ge_{1.94(1)} single crystal, normalized to the 290 K value. The upper inset shows the expanded view at low temperatures, where superconductivity below $T_C = 2.1$ K is clearly seen. The lower inset presents the bulk magnetic susceptibility at low field and low temperatures, showing that the bulk magnetization traces the superconductivity deduced from the lossless conductivity.

4.3. Superconductivity

Lu[Bi_xGe_{1-x}]₂ is non-magnetic, as expected for the heaviest rare-earth element with completely filled *f*-orbitals. Fig. 10 shows the temperature dependence of the electrical resistivity of this sample. At temperature below $T_C = 2.1$ K, the compound becomes a superconductor as detected by both resistivity and bulk magnetic susceptibility (χ) measurements. Superconductivity has been found to disappear above an external magnetic field of only 100 G in the (χ - T) measurement (not shown), indicating a conventional type superconductor. The “parent” compound LuGe₂ has been reported to be a superconductor below $T_C = 2.6$ K [15], thus the small substitution of Ge with Bi apparently suppresses T_C . It should be noted here that no superconducting transition above 1.8 K was observed for the nonstoichiometric compound LuGe_{1.5} with AlB₂-type structure [15].

5. Conclusions

An extended series of rare-earth metal–bismuth–germanides RE[Bi_xGe_{1-x}]₂ ($RE = Y, Pr-Sm, Gd-Tm, Lu$) have been synthesized and characterized. They crystallize with the same extended symmetry (space group *Cmcm*), but the structures can be divided into three groups, which are correlated by the transformation and the arrangement of the disordered $1_{\infty}[Ge_2]$ chains. The magnetization measurements showed low-temperature antiferromagnetic order and suggested the RKKY exchange interaction in most compounds. The *s*-*f* coupling and RKKY mediated Heisenberg exchange interactions, evaluated based on the mean-field theory, were used to understand their magnetic behaviors. RE[Bi_xGe_{1-x}]₂ are the first compounds between these elements, so far, demonstrating the potential for pursuing further exploratory work in these systems.

Acknowledgments

Svilen Bobev acknowledges financial support from the National Science Foundation through a Grant DMR-0743916 (CAREER). Work at the University of Maryland was supported by AFOSR-Multidisciplinary University Research Initiative Grant no. FA9550-09-1-0603.

Appendix A. Supporting information

Supplementary data associated with this article can be found in the online version at doi:10.1016/j.jssc.2012.07.031. The information consists of a table with the data collection and structure refinement parameters for DyBiGe prepared via stoichiometric reaction and annealing; representative results from EDX analyses, a figure showing detailed views of the differences in the orientations of the Ge zig-zag chains in the $RE[Bi_xGe_{1-x}]_2$ structures ($RE=Pr, Gd$ —structure I, and $RE=Dy$ —structure II).

References

- [1] [a] K.A. Gschneidner Jr., L. Eyring (Eds.), Handbook on the Physics and Chemistry of Rare Earths, North Holland, Amsterdam, Vols. 1, 2, 17, 19, 1978, the references therein;
- [b] K.H.J. Buschow, Rep. Prog. Phys. 42 (1979) 1373, and the references therein;
- [c] A. Szytula, J. Leciejewicz (Eds.), Handbook of Crystal Structures and Magnetic Properties of Rare Earth Intermetallics, CRC Press, Boca Raton, FL, 1994, the references therein.
- [2] [a] P. Rogl, B. Chevalier, J. Etourneau, J. Solid State Chem. 88 (1990) 429;
- [b] A.M. Guloy, J.D. Corbett, Inorg. Chem. 32 (1993) 3532;
- [c] G. Venturini, I. Ijjaali, B. Malaman, J. Alloys Compd. 285 (1999) 194;
- [d] A. Grytsiv, D. Kaczorowski, A. Leithe-Jasper, P. Rogl, C. Godart, M. Potel, H. Noël, J. Solid State Chem. 163 (2002) 37;
- [e] M.J. Evans, Y. Wu, V.F. Kranak, N. Newman, A. Reller, F.J. Garcia-Garcia, U. Häussermann, Phys. Rev. B 80 (2009) 064514;
- [f] N. Nasir, N. Melnychenko-Koblyuk, A. Grytsiv, P. Rogl, G. Giester, J. Wosik, G.E. Nauer, J. Solid State Chem. 183 (2010) 565;
- [g] A.V. Morozkin, R. Nirmala, O. Isnard, S.K. Malik, J. Yao, Yu. Mozharivskiy, S.A. Granovsky, Intermetallics 12 (2011) 1794;
- [h] J. Yao, Yu. Mozharivskiy, Z. Anorg. Allg. Chem. 637 (2011) 2039;
- [i] F. Wrubl, K.V. Shah, D.A. Joshi, P. Manfrinetti, M. Pani, C. Ritter, S.K. Dhar, J. Alloys Compd. 509 (2011) 6509;
- [j] S.P. Guo, T.S. You, S. Bobev, Inorg. Chem. 51 (2012) 3119.
- [3] T.B. Massalski (Ed.), American Society for Metals, Materials Park, OH, 1990.
- [4] [a] V.N. Eremenko, V.G. Batalin, Yu.I. Buyanov, I.M. Obushenko, Dop. Akad. Nauk. Ukr. RSR. B 6 (1977) 516G;
- [b] Venturini, I. Ijjaali, B. Malaman, J. Alloys Compd. 284 (1999) 262;
- [c] O. Oleksyn, P. Schobinger-Papamantellos, C. Ritter, C.H. de Groot, K.H.J. Buschow, J. Alloys Compd. 262–263 (1997) 492.
- [5] J.H. Westbrook, R.L. Fleischer (Eds.), Intermetallic Compounds Vol. 1: Crystal Structures of Intermetallic Compounds, John Wiley & Sons, New York, 2000. (Chapter 1).
- [6] P.T. Tobash, J.J. Meyers, G. DiFilippo, S. Bobev, F. Ronning, J.D. Thompson, J.L. Sarrao, Chem. Mater. 20 (2008) 2151.
- [7] [a] P.C. Canfield, Z. Fisk, Phil. Magn. B65 (1992) 1117;
- [b] M.G. Kanatzidis, R. Pöttgen, W. Jeitschko, Angew. Chem., Int. Ed. 44 (2005) 6996.
- [8] L. Pauling, The Nature of the Chemical Bond, Cornell University Press, Ithaca, NY, 1960.
- [9] P.H. Tobash, D. Lins, S. Bobev, A. Lima, M.F. Hundley, J.D. Thompson, J.L. Sarrao, Chem. Mater. 17 (2005) 5567.
- [10] P.H. Tobash, G. DiFilippo, S. Bobev, J.D. Hur Namjung, J.L. Thompson, Sarrao, Inorg. Chem. 46 (2007) 8690.
- [11] [a] Bruker-SMART, Bruker AXS Inc., Madison, WI, USA, 2003.;
- [b] Bruker-SMART, Bruker AXS Inc., Madison, WI, USA, 2003.
- [12] SADABS, Bruker AXS Inc., Madison, WI, USA, 2003.
- [13] SHEXLTL, Bruker AXS Inc., Madison, WI, USA, 2003.
- [14] CIFs have also been deposited with Fachinformationszentrum Karlsruhe, 76344 Eggenstein-Leopoldshafen, Germany (Fax: +49 7247 808 666; e-mail: crysdata@fiz.karlsruhe.de) with depository numbers: CSD-424791 for YBi0.11(1)Ge1.75(2), CSD-424792 for PrBi0.31(1)Ge1.63(1), CSD-424793 for NdBi0.28(1)Ge1.62(1), CSD-424794 for SmBi0.26(1)Ge1.64(2), CSD-424795 for GdBi0.21(1)Ge1.69(2), CSD-424796 for TbBi0.14(1)Ge1.74(1), CSD-424797 for DyBi0.10(1)Ge1.75(1), CSD-424798 for HoBi0.08(1)Ge1.77(2), CSD-424801 for ErBi0.16(1)Ge1.84(1), CSD-424799 for TmBi0.11(1)Ge1.89(1), and CSD-424800 for LuBi0.06(1)Ge1.94(1).
- [15] Y.R. Chung, H.H. Sung, W.H. Lee, Phys. Rev. B 70 (2004) 052511.
- [16] P.H. Tobash, S. Bobev, F. Romming, J.D. Thompson, J.L. Sarrao, J. Alloys Compd. 488 (2009) 511.
- [17] P. Villars, L.D. Calvert (Eds.), Pearson's Handbook of Crystallographic Data for Intermetallic Compounds, second ed., American Society for Metals, Materials Park, OH, USA (and the desktop edition, 1997), 1991.
- [18] [a] J.K. Burdett, S.J. Lee, J. Am. Chem. Soc. 105 (1983) 1079;
- [b] W. Tremel, R. Hoffmann, J. Am. Chem. Soc. 109 (1987) 124.
- [19] Naturally, the ${}^2_{\infty}[M]$ sheets in the next unit must be shifted half a unit in the diagonal direction of ${}^2_{\infty}[M]$ sheets, otherwise the unit cell would not have to be enlarged, a direct consequence of the doubled cell parameter in the longest axis.
- [20] J.H. Van Vleck, The Theory of Electric and Magnetic Susceptibilities, Oxford University Press, London, 1965.
- [21] A.M. Stewart, Phys. Rev. B 6 (1972) 1985.
- [22] [a] A. Brown, Acta Cryst. 14 (1961) 860;
- [b] A. Brown, Acta Cryst. 15 (1962) 652;
- [c] K. Sekizawa, J. Phys. Soc. Jpn. 21 (1966) 1137.
- [23] P.G. de Gennes, J. Phys. Radium 23 (1962) 510.
- [24] [a] A.P. Murani, J. Phys. C: Metal. Phys. Suppl. (No. 2) (1970) S153;
- [b] A.M. Stewart, J. Phys. F: Metal. Phys. 3 (1973) 1024.
- [25] L. Néel, Nuovo Cimento Suppl. 6 (1957) 942.
- [26] [a] O. Oleksyn, P. Schobinger-Papamantellos, C. Ritter, Y. Janssen, E. Bruck, K.H.J. Buschow, J. Phys.: Condens. Matter 9 (1997) 9993;
- [b] T. Kasuya, Prog. Theor. Phys. 16 (1956) 45.
- [27] A. Aharoni, Introduction to the Theory of Ferromagnetism, Oxford University Press, New York, 1996. (Chapter 2).
- [28] X. Lu, L. Zeng, K. Shih, Mater. Chem. Phys. 130 (2011) 1336.
- [29] T.M. Dunn, D.S. McClure, R.G. Pearson, Some Aspects of Crystal Field Theory, Harper & Row, New York, 1965.
- [30] B. Bersuker, Electronic Structure and Properties of Transition Metal Compounds: Introduction to the Theory, second ed., John Wiley & Sons, Inc., 2010. (Chapter 4).

Supporting information

New rare-earth metal germanides with bismuth substitution.

Synthesis, structural variations, and magnetism of the

$RE[Bi_xGe_{1-x}]_2$ ($RE = Y, Pr, Nd, Sm, Gd-Tm, Lu$) compounds

Figure S1. Plot of EDX-established compositions for several PrBiGe single-crystals (square represents Ge, circle Pr and triangle Bi, respectively).

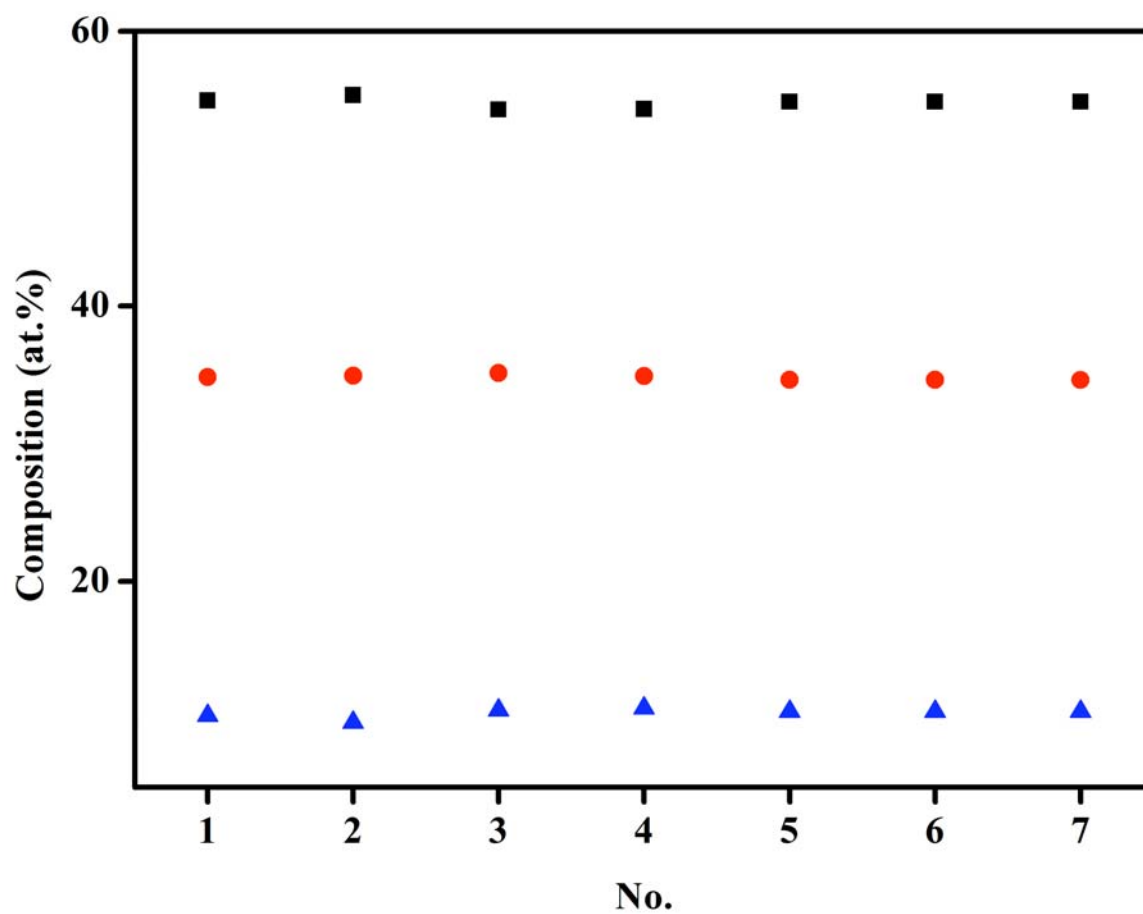


Figure S2. A magnified view of the surface of one of the PrBiGe single-crystals, selected randomly, alongside the corresponding elemental mappings.

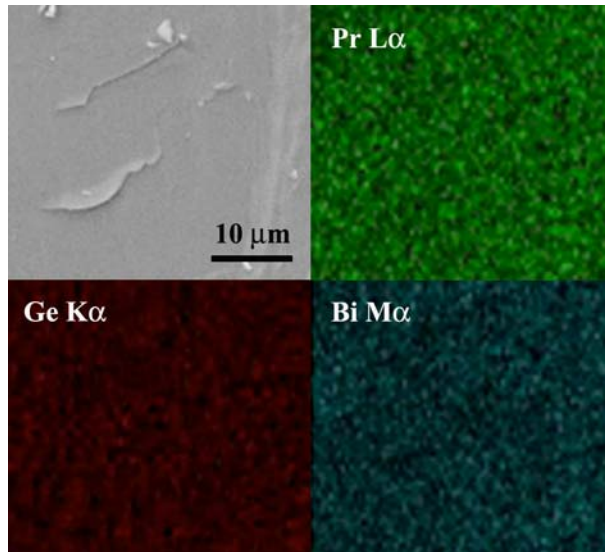


Figure S3. Close-up views of the different orientations of the Ge zigzag chains in the $RE[Bi_xGe_{1-x}]_2$ structures ($RE = Pr, Gd$ —structure I, and $RE = Dy$ —structure II). The refined atomic positions in the disordered Ge zigzag chains are marked.

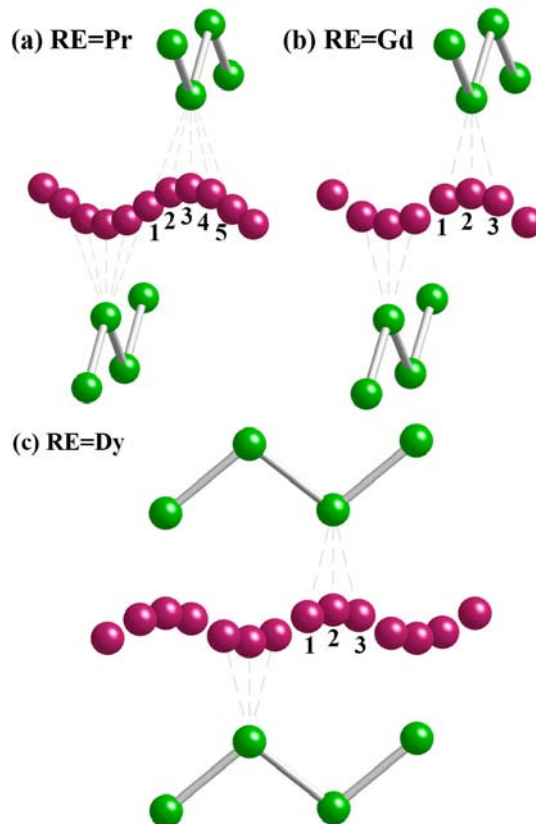


Table S1. Single-crystal data collection and structure refinement parameters for DyBiGe produced by induction melting and subsequent annealing

Empirical formula	DyBi _{0.13(2)} Ge _{1.73(2)}
Formula weight	315.59
Space group	<i>Cmcm</i> (No. 63), Z=8
Radiation, λ	Mo K α , 0.71073 Å
Temperature	-153 °C
Unit cell parameters	
a /Å	4.132(1)
b /Å	30.017(7)
c /Å	3.9357(9)
V /Å ³	488.2(2)
ρ_{calc} /g cm ⁻³	8.588
μ /cm ⁻¹	605.6
Data : parameters ratio	460:28
Final R1 ($I > 2\sigma_I$)	R1=0.0301, wR2=0.0643
Largest diff. peak & hole /e ⁻ Å ⁻³	2.037 & -4.140